Limits to Mercury's magnesium exosphere from MESSENGER second flyby observations

Menelaos Sarantos[a,b,*], Rosemary M. Killen[c], William E. McClintock[d], E. Todd Bradley[e], Ronald J. Vervack, Jr.[f], Mehdi Benna[b,g], and James A. Slavin[a]

[a] Heliophysics Science Division, NASA Goddard Space Flight Center, Greenbelt, MD 20771, USA

[b] Goddard Earth Sciences and Technology Center, University of Maryland, Baltimore County, Baltimore, MD 21228, USA

[c] Planetary Magnetospheres Branch, NASA Goddard Space Flight Center, Greenbelt, MD 20771, USA

[d] Laboratory for Atmospheric and Space Physics, University of Colorado, Boulder, CO 80303, USA

[e] Department of Physics, University of Central Florida, Orlando, FL 32816, USA

[f] The Johns Hopkins University Applied Physics Laboratory, Laurel, MD 20723, USA

[g] Solar System Exploration Division, NASA Goddard Space Flight Center, Greenbelt, MD 20771, USA

*Corresponding author. Fax: +1 301 286 1648. Phone: +1 301 286 2945

E-mail address: menelaos.sarantos-1@nasa.gov

Abstract

The discovery measurements of Mercury's exospheric magnesium, obtained by the MErcury Surface, Space ENvironment, GEochemistry, and Ranging (MESSENGER) probe during its second Mercury flyby, are modeled to constrain the source and loss processes for this neutral species. Fits to a Chamberlain exosphere reveal that at least two source temperatures are required to reconcile the distribution of magnesium measured far from and near the planet: a hot ejection process at the equivalent temperature of several tens of thousands of degrees K, and a competing, cooler source at temperatures as low as 400 K. For the energetic component, our models indicate that the column abundance that can be attributed to sputtering under constant southward interplanetary magnetic field (IMF) conditions is at least a factor of five less than the rate dictated by the measurements. Although highly uncertain, this result suggests that another energetic process, such as the rapid dissociation of exospheric MgO, may be the main source of the distant neutral component. If meteoroid and micrometeoroid impacts eject mainly molecules, the total amount of magnesium at altitudes exceeding ~100 km is found to be consistent with predictions by impact vaporization models for molecule lifetimes of no more than two minutes. Though a sharp increase in emission observed near the dawn terminator region can be reproduced if a single meteoroid enhanced the impact vapor at equatorial dawn, it is much more likely that observations in this region, which probe heights increasingly near the surface, indicate a reservoir of volatile Mg being acted upon by lower-energy source processes.

45 *Keywords*:

46 Mercury

47 Mercury atmosphere

48 Mercury surface

49 Atmospheric structure

50 Mercury magnetosphere

51 MESSENGER

52

52

53 **1. Introduction**

54

55 Mercury is enveloped by a rarefied collisionless exosphere whose source is largely
56 the surface of the planet itself, which is continuously being bombarded by a flux of
57 micrometeoroids, solar-wind ions, and ultraviolet (UV) photons. Known exospheric
58 constituents include H, He, Na, K, O, and Ca (e.g., Killen et al., 2007), and Mg, which
59 was recently discovered by the MErcury Surface, Space ENvironment, GEochemistry,
60 and Ranging (MESSENGER) spacecraft (McClintock et al., 2009). Because the
61 exosphere reflects a combination of surface composition, the composition of vaporizing
62 micrometeoroids, and the escape rates of atoms from the various source processes, we
63 expect the detection of other atomic and molecular constituents of Mercury's exosphere
64 by MESSENGER (Solomon et al., 2001) and by future missions such as BepiColombo
65 (Milillo et al., 2010).

66 On its way to insertion into orbit around Mercury in 2011, MESSENGER flew by the
67 planet three times, on January 14, 2008, October 6, 2008, and September 29, 2009.
68 During the first of these encounters (M1), the Ultraviolet and Visible Spectrometer
69 (UVVS) channel on the Mercury Atmospheric and Surface Composition Spectrometer
70 (MASCS) instrument on MESSENGER observed the planet's exosphere at the resonant
71 emission lines of Na (589.0 and 589.5 nm), Ca (422.7 nm), and H (121.6 nm)
72 (McClintock et al., 2008). During the second (M2) and third (M3) flybys, UVVS also
73 observed the Mg (285.2 nm) line (McClintock et al., 2009; Vervack et al., 2010).
74 MESSENGER probed the nightside (tail) and terminator exospheric regions with

75 unprecedented spatial coverage but did not observe the dayside exosphere (except for H).
76 These observations revealed substantial differences even for chemically related species.
77 Calcium appeared to peak near the equatorial dawn flank during all three flybys, sodium
78 was enhanced at high latitudes, and magnesium appeared to be uniformly distributed
79 during M2 but enhanced above the northern pole during M3.

80 The differences in the distributions of individual species point to differing ejection
81 mechanisms and relate, perhaps, to different regions of surface composition and/or
82 mechanisms of global circulation and surface replenishment. Sodium has been the most
83 extensively studied species because its favorable spectroscopic properties enable its long-
84 term monitoring from Earth, yet the relative importance of several proposed source
85 processes is still under debate (e.g, Killen et al., 2001; Killen et al., 2004, Mura et al.,
86 2009) and their interplay may exhibit an annual trend (Leblanc and Johnson, 2010). At
87 the time of the MESSENGER flybys, the main source of low-latitude sodium production
88 was found to be photon-stimulated desorption (PSD); the efficiency of this source was
89 enhanced at high latitudes by solar wind precipitation (Burger et al., 2010); finally, the
90 dayside content was consistent with a moderate degree of thermal accommodation upon
91 interaction with the surface (Mouawad et al., 2011). Although the calcium distribution
92 obtained by MESSENGER remains unexplained, its high temperature in the tail is
93 consistent with the possible photodissociation of an exospheric molecule such as CaO as
94 suggested by ground-based observations (Killen et al., 2005).

95 The measurements of Mg by MESSENGER were first analyzed by Killen et al.
96 (2010). They showed that the observed magnesium tail was hotter than can be expected
97 by direct impact vaporization, and they attributed these high temperatures (>10,000 K) to

98 vaporization of ~30% of the magnesium vapor in molecular form (MgO) followed by its
99 dissociation. They noted that the exospheric temperature was poorly constrained, even
100 more so near the planet, where no single temperature could be made to fit. In this paper
101 we elaborate upon the Killen et al. (2010) analysis using a large number of simulations
102 that seek to constrain many unknown physical constants for this species, such as the
103 lifetime of the proposed molecule, the inferred exospheric source rates, and the relation
104 between the exosphere and the surface content. In Sections 2 and 3 we describe the
105 observational sequence, we analyze the measurements using a Chamberlain (1963) model,
106 and we provide evidence of multiple source components and rates. In Section 4 we detail
107 our exosphere model assumptions and place limits on the possible contributions from
108 several proposed source processes of exospheric magnesium: (1) solar-wind ion
109 sputtering in polar areas that are only partially shielded by the planetary magnetic field,
110 (2) production of magnesium atoms due to micrometeoroid impact vaporization, and (3)
111 dissociation of a Mg-bearing molecule such as MgO with a finite lifetime. In Section 5
112 we demonstrate that low-altitude data obtained near the dawn terminator strongly suggest
113 the presence of either an additional local source or, more likely, a source that is colder
114 than impacts or sputtering. The paper concludes with a summary of the major findings in
115 Section 6.
116
117 **2. Observations of magnesium during the second MESSENGER flyby**

Sean Solomon 3/4/11 9:16 AM
Comment:

118
119 During the second MESSENGER flyby, the UVVS spectrometer scanned Mercury's
120 exosphere at the Mg 285.2-nm line with a 0.1° × 1° field of view. The measurements,

121 detailed by McClintock et al. [2009], were organized spatially and temporally in the
122 following sequence:
123
124 • As the spacecraft approached Mercury and at downstream distances between 14
125 R_M and 2 R_M (where R_M is Mercury's radius, or 2,440 km), both the equatorial and
126 the high-latitude neutral tail were observed.
127 • While inside Mercury's shadow (and near closest approach), the spacecraft
128 executed a ~180° roll, initially pointing toward dawn, then rotating through north
129 toward the dusk direction, while moving toward the planet from about 3,000 km
130 (1.2 R_M) to within 450 km (0.2 R_M) above the planetary surface.
131 • As the spacecraft exited the shadow past closest approach and at distances ≤ 1,000
132 km, the lines of sight pointed toward the planetary shadow and intersected the
133 surface in the equatorial near-nightside and dawn terminator regions.
134
135 In what follows we refer to the set of observations obtained first upon initial approach to
136 Mercury as "tail measurements," to the set of observations obtained second during the
137 spacecraft roll as "fantail measurements," and to the third and final set as "near-
138 terminator measurements." Observations of magnesium on the dayside were not
139 conducted during the flybys. The excitation mechanism is presumed to be resonant
140 scattering of sunlight. Hence, the instrument sees that portion of the exosphere that is
141 illuminated, i.e., outside Mercury's shadow.
142 Excepting the shadow, the tail and fantail lines of sight probed exospheric material
143 from the spacecraft to infinity. During these two sequences the closest tangent point
144 outside the shadow was ~1100 km above the surface. Because the minimum ejection
145 speed for a magnesium atom to reach this altitude is 2.3 km/s, or ~50% of the escape
146 velocity, these lines of sight survey energetic atoms. In marked contrast, the

147 measurements near the dawn terminator probed material much closer to the surface, with
148 lines intercepting the shadow at progressively diminishing heights, starting at 162 km
149 altitude and eventually reaching the surface. Obviously, a wider spectrum of ejection
150 speeds can populate these altitudes compared to altitudes scanned by the tail and fantail
151 observations. Another difference is that lines of sight near the terminator are only 200–
152 800 km long (i.e., from the spacecraft to the shadow or surface).
153
154 **3. Fits to a Chamberlain exosphere**
155
156 In order to remove geometrical effects, the exospheric measurements were first fit to a
157 Chamberlain (1963) model. The instrument measures intensity,
158 $$4\pi I = gN_{LOS} = \int_{R_{SP}}^{\infty} g(\mathbf{r})n(\mathbf{r})\, ds, \qquad (1)$$
159 where g is the emission probability (photons s^{-1} $atom^{-1}$) at the relevant Doppler-shifted
160 resonance line, N_{LOS} is the column abundance, $\mathbf{r}$ is the radius vector from the planet
161 center, s is the distance along the line of sight (LOS) from the spacecraft location R_{SP} to
162 infinity (or to the shadow in the case of the measurements near the terminator), and the
163 neutral density n is a function of altitude and source temperature. Two model free
164 parameters must be determined by least squares fitting of the model to the data weighted
165 by the measurement uncertainty: the temperature, T, and the surface density, n_0, of the
166 source. We have run models having with exobase temperatures between 100 K and
167 50,000 K and have excluded from the model intensities, I, the portion lying inside the
168 planetary shadow.
169 Comparisons of modeled and observed magnesium in the tail regions are presented in
170 Fig. 1, followed, in Fig. 2, by fits of the fantail and near-terminator measurements. The

171 modeled column abundances were converted to line intensity using a g–factor for Mg at
172 285.2 nm of g_{Mg} = 0.317 photons s^{-1} $atom^{-1}$ given Mercury's radial velocity of v_r = - 9.2
173 km/s during the flyby (Killen et al., 2009, 2010). The tail data (Fig. 1) are ordered by the
174 distance $-x$ downstream of Mercury where each line of sight intercepts the noon–midnight
175 meridian (x-z) plane, and by the distance z of this intercept above the equatorial plane.
176 The fantail data (Fig. 2a) are shown versus the boresight angle with respect to dawn
177 (where dawn = 0° and north = 90°), and the near-terminator lines (Fug. 2b) are plotted
178 against the spacecraft altitude from the planetary shadow. The best-fit parameters, n_0 and
179 T, for each model, along with the reduced chi-squared error, χ^2/ν (where ν is the number
180 of measurements minus two) and the corresponding production rate of magnesium atoms,
181 $S = \frac{n_0}{2\sqrt{\pi m / 2K_B T}}$, for an assumed Maxwellian velocity distribution (where m is the
182 mass of a magnesium atom and K_B is the Boltzmann constant), were computed using all
183 ~200 lines of sight.

184 [Insert Fig.1; Fig.2]

185 Inspection of Figs. 1 and 2 leads to the following conclusions:

186 1) A single "warm" ($T \leq$ 10,000 K) source underestimates the tail measurements
187 and overestimates data near the planet.
188 2) A single hot source can describe measurements obtained far from the planet
189 with production rate ~(8–15) × 10^5 atoms cm^{-2} s^{-1}. Models having
190 temperatures ≥ 20,000 K are indistinguishable given the uncertainty in the
191 measurements (see Figs. 1 and 2).

3) No single temperature can describe the data near and far from the planet in an internally consistent manner. The rates and temperatures needed to fit the tail measurements underestimate the magnesium abundance near the surface.

These remarks effectively summarize the conclusions of the analysis by Killen et al. (2010). The improvement up to this point is that we have fit all measurements together here, a treatment that accentuates the conclusion of several distinct components.

In Fig. 3 we have fit the measurements in the weighted least-squares sense to a two-component Chamberlain model, $I(\mathbf{r}) = n_{0,\mathrm{LT}}\, I(\mathbf{r}, T_{\mathrm{COOL}}) + n_{0,\mathrm{HT}}\, I(\mathbf{r}, T_{\mathrm{HOT}})$, where $n_{0,\mathrm{LT}}$ ($n_{0,\mathrm{HT}}$) and T_{COOL} (T_{HOT}) are the surface density and temperature, correspondingly, of the cool (hot) components of the exosphere. In this case the added constraint of non-negative surface densities must be enforced in minimizing the squared residuals in order to obtain physically meaningful solutions. We have found that the superposition of a hot source ($T_{\mathrm{HOT}} \geq 20{,}000$ K) with a cooler source ($T_{\mathrm{COOL}} \leq 5000$ K) improves the description near dawn compared to residuals obtained with a single-component model (e.g., compare Figs. 2 and 3a-b and the related χ^2/ν error shown in Table 1 when $T_{\mathrm{COOL}} = 3000$ K is assumed). In particular, Figs. 3c-d demonstrate that the exospheric signature at low altitudes is reproduced best if $T_{\mathrm{COOL}} = 400$ K is assumed, which describes thermalized ejecta (also see Table 1). At $T = 400$ K the mean velocity of a magnesium atom leaving the surface is 1 km/s, so the altitude reached is ~152 km. Such a low-energy source is undetectable given only tail and fantail measurements, and lies below the scale of Fig. 3c.

[Insert Figure 3; Insert Table 1]

In conclusion, Chamberlain models indicate that at least two distinct temperatures and source rates of a few times 10^6 atoms $\mathrm{cm}^{-2}\ \mathrm{s}^{-1}$ are required to fit the data. In the next

215 section we investigate the kinds of physical processes that might be consistent with these
216 requirements.
217
218 **4. Relative roles of sources populating the magnesium tail**
219
220 *4.1. Model formulation*
221
222 Mercury's neutrals are subject to losses via ballistic escape, radiation acceleration
223 (strong for Na, weak for Ca, and negligible for Mg), adsorption upon surface impact, and
224 photoionization. Thus, they are continuously resupplied by the surface via a number of
225 processes, including photon-stimulated desorption and thermal desorption that act upon
226 volatiles, as well as micrometeoroid impact vaporization and sputtering by the solar wind
227 and recycled magnetospheric ions that act upon both volatile and refractory species (e.g.,
228 Killen et al., 2007).
229 Near Mercury the magnesium neutrals are subjected only to gravitational forces,
230 because for this species the radiation pressure is a very small fraction of Mercury's
231 gravity and the photoionization lifetime is ~ 57 h (McClintock et al., 2009). Hence, the
232 magnesium production and its distribution are modeled with an analytical model of
233 particle transport in a collision-free exosphere (Hartle, 1971). The model uses Liouville's
234 theorem to compute the density of neutrals,
235 $$n(\mathbf{r}) = \int f(\mathbf{r},\mathbf{v}) d^3\mathbf{v}, \qquad (2)$$
236 at an exospheric location $\mathbf{r}$, where f is a truncated distribution function relating the
237 constants of motion in a gravitational field to $f_0(\mathbf{r_0},\mathbf{v_0})$, the velocity distribution
238 function of released particles from the surface. Prior to applying it to the study of

239 magnesium transport at Mercury, we modified this model to simulate the velocity
240 distribution function of sputtered particles, we used it to describe the source rates of the
241 lunar sodium exosphere, and we validated it against ground-based observations (Sarantos
242 et al., 2010).
243
244 *4.1.1. Exospheric sources*
245
246 The sources we initially considered are the typical processes that have been
247 hypothesized to produce exospheric refractory gases: impact vaporization, sputtering, and
248 molecular dissociation. However, we later allowed for the possibility of less energetic
249 sources acting upon a limited reservoir of volatile particles because we found that low-
250 altitude data could not be reproduced by high-energy sources. Source processes can be
251 co-added because of the collisionless nature of the exosphere, but they compete for the
252 same surface reservoir. Thermal processes act upon the top monolayer; sputtering affects
253 the top ~10 nm, and impacts tap the top 1 μm or more of the surface.
254 Sputtering by solar wind ions is a potential source of energetic atoms. Originally
255 introduced to explain the rapid temporal variability and the high-latitude enhancements
256 seen in Mercury's sodium exosphere (e.g., Killen et al., 2001), this source is regulated by
257 the interaction of the solar wind with the magnetosphere formed by Mercury's planetary
258 magnetic field. The fraction of the surface that can be exposed to solar wind ions varies
259 in response mainly to changes in the interplanetary magnetic field (IMF) (e.g., Sarantos et
260 al., 2001; Sarantos et al., 2007). The rate for this source is proportional to three uncertain
261 parameters: the abundance of magnesium in the regolith, the sputtering yield per incident
262 ion, and the influx onto Mercury's surface and composition of the solar wind.

Sean Solomon 7/6/11 8:16 AM
Comment: Menelaos, is this OK?

263 Impact-driven vaporization caused by micrometeoroids is expected to be a source of
264 exospheric atoms (e.g., Morgan et al. 1988; Cintala 1992; Morgan and Killen, 1997,
265 Killen et al., 2001). The amount of vapor produced in this way is proportional to the
266 influx of micrometeoroids and depends on their velocity distribution. The mean impact
267 velocity may exceed 20 km/s at Mercury's orbit, and is even higher than that for larger
268 meteoroids or during meteoroid streams. Possible temperatures for impact vaporization
269 ejecta of 2500-5000 K, depending on the impact energy and the thermophysical
270 properties of the target material, are obtained in hypervelocity impact experiments
271 (Eichhorn, 1978). Uncertainties in the physical properties of the regolith and the
272 impactors, the assumed micrometeoroid mass flux and velocity, and the method used to
273 calculate the vapor yields each contribute to roughly a factor of five uncertainty in the
274 estimated vapor production rates (e.g., Cintala, 1992; Killen et al., 2005).

275 Molecules can be produced in the vapor + liquid + solid phase that follows
276 micrometeoroid impact. According to quenching theory, chemical reactions during the
277 collisional phase of the cloud (10^{-7} – 10^{-5} s) lead to the formation of metallic oxides and
278 hydroxides (e.g., MgO, CaO, CaOH) (Berezhnoy and Klumov, 2008; Berezhnoy, 2010).
279 Such molecules may photolyze or dissociate due to their high internal energy and
280 produce high-energy atoms of Mg, Ca, O, as well as other species. We adopt the premise
281 that a dissociating molecule is a major source of energetic atomic Mg (Killen et al., 2010).
282 The same mechanism has been suggested by Killen et al. (2005) to be the main reason
283 why Mercury's neutral Ca tail is extremely hot. Besides the uncertainty in total impact
284 vapor, the unknowns for this source include the abundance ratio of atoms versus
285 molecules of the same species in the vapor cloud, and the molecular dissociation lifetime
286 and temperature.

287 Although less energetic sources such as photon-stimulated desorption or thermal
288 desorption cannot act on intrinsic magnesium that is bound in silicate phases, such
289 processes could act on recycled, gravitationally returning atoms that were originally
290 vaporized from silicates by impacts and sputtering. The main uncertainty here is whether
291 reabsorbed Mg physisorbs, or weakly adsorbs to the surface following return, so that
292 lower energy processes can re-eject them to the gas phase. The rate for low-energy
293 sources cannot exceed the return rate of atoms delivered by energetic processes, which
294 can be constrained from high-altitude measurements.
295
296 *4.1.2. Exospheric sinks*
297
298 Our model explicitly accounts for losses due to ballistic escape and sticking. Each
299 returning atom is assumed to stick with unit efficiency. For those atoms that are
300 generated by a dissociating molecule we also include losses due to the formation of a
301 stable molecule with a finite lifetime (Section 4.4). However, the possible role of the
302 surface as a sink requires some discussion.
303 Previous investigations have demonstrated that the efficiency of exospheric Na
304 ejection is related to a surface reservoir whose content varies with distance from the Sun.
305 A complex balance between the exospheric and the surface supply arises because (1) the
306 dayside reservoir for the very efficient processes (e.g., thermal vaporization and PSD)
307 can become depleted in local time if the resupply rate is not sufficiently large (Leblanc
308 and Johnson, 2010); (2) the resupply rate is diffusion-limited (Killen et al., 2004; Burger
309 et al., 2010); and (3) solar wind precipitation may enrich the surface by enhancing
310 diffusion through creation of vacancies (Mura et al., 2009; Burger et al., 2010). In

311 sodium simulations by Leblanc and Johnson (2010) and Mura et al. (2009), each test
312 particle is tracked even when trapped at the surface.

313 Unlike Na, which is a trace species of the regolith, observations of Mg by
314 MESSENGER allow us to infer that the regolith turnover rate ("gardening rate") can
315 most likely provide sufficient fresh targets to populate the exosphere with this species.
316 We demonstrate that only if the impact vapor consists mainly of molecules with half-
317 lives in excess of ~2 min do the required source rates approach the gardening rate
318 (Section 4.4). Otherwise, our results suggest that, to first order, the Mg surface supply for
319 hot processes can be treated as infinite. However, what is limited is a possible reservoir
320 of volatiles which may be needed to explain the measurements at low altitudes (Sections
321 3 and 5.2). Therefore, we assume in our simulations two populations of Mg at the
322 surface: one that is strongly bound in silicate phases and can be released only by impacts
323 and sputtering, and one that originates from atoms and molecules that have returned to
324 the surface following emission from the silicate population. The latter component should
325 physisorb with lower binding energy than Mg in silicates so that it can be vaporized by
326 lower-energy processes.

Sean C. Solomon 3/4/11 5:10 PM
Comment: Menelaos, I can't understand this sentence. What is a "thermal particle"? What is your "evidence"?

Menelaos Sarantos 3/4/11 5:16 PM
Comment: Sean, "volatiles" has substituted "thermal particles". Elsewhere, "thermal processes" are now referred to "low-energy" or "less energetic" processes. I've added the Section numbers where this "evidence" is presented.

327

328 *4.2. Ion sputtering*

329

330 Simulations of sputtered magnesium are initialized with the flux of precipitating solar
331 wind ions predicted by a magnetohydrodynamic (MHD) model of Mercury's
332 magnetosphere (Benna et al., 2010). The model predictions under the southward IMF **B**
333 field that prevailed during the second MESSENGER flyby are shown in Fig. 4a. The
334 assumed solar-wind conditions were: $n_{sw} = 20$ cm^{-3}, $V_{sw} = 400$ km/s, and $[B_x, B_y, B_z] = [-$

335 8, 4, -10] nT, where n_{sw} and V_{sw} are the solar wind density and velocity, respectively, and
336 the IMF is given in Mercury solar orbital coordinates, where x is directed from the center
337 of the planet toward the Sun, z is normal to Mercury's orbital plane and toward the north
338 celestial pole, and y is in the direction opposite to orbital motion.

339 The production rate due to ion sputtering is obtained by assuming a sputtering yield,
340 Y, weighted by protons and alpha particles, of 0.1 per ion impact (Wurz et al., 2007), an
341 upper limit for the magnesium abundance in the regolith of $c = 0.17$ by number (Wurz et
342 al., 2010), and a precipitating flux of $F_{SW} = 2 \times 10^8$ solar wind ions cm^{-2} s^{-1} poleward of
343 ±50° dayside latitude. These parameters yield a sputtered flux, $F_{SPUTT} = cYF_{SW}$, of 3.6 ×
344 10^6 Mg atoms cm^{-2} s^{-1} and a modeled near-surface density, n_0, of ~6 atoms cm^{-3} at polar
345 cusp latitudes. The mean ejection energy for this process is approximately half the
346 binding energy, which is assumed to be 3.6 eV in this simulation, and the energy, E, and
347 directionality of the ejecta are described by the Sigmund-Thompson function (e.g., Wurz
348 et al., 2007):

349 $$f(E,\delta) = \frac{6E_b}{3-8\sqrt{E_b/E_{Max}}} \frac{E}{(E+E_b)^3} \{1-\sqrt{(E+E_b)/E_{Max}}\} \cos\delta \qquad (3)$$

350 where $E_b = 3.6$ eV the magnesium binding energy to the regolith grains, $E_{Max} = 450$ eV
351 the maximum energy that can be imparted to the ejected magnesium atoms by 3 keV
352 protons, and δ the angle from local vertical. Due to the effects of soil porosity, the atoms
353 are sputtered primarily perpendicular to the surface, with the yield assumed to lessen as
354 cos δ.

355 Subject to these assumptions, our simulations demonstrate that the contribution by
356 sputtering to the fantail measurements varies from about 10% for observations near the
357 equator to about 50% for those over the northern pole (Fig. 4b). On average, about 20%

358 of the column abundance observed during these measurements can be attributed to
359 sputtering.
360 [Insert Fig. 4]
361 These predictions are uncertain for two reasons. First, the predicted location and flux
362 of the plasma reaching the surface are not only model-dependent but are also sensitive to
363 the assumed solar wind conditions. These conditions can be inferred only indirectly
364 because MESSENGER observes neither the solar wind nor the IMF while inside the
365 magnetosphere. More importantly, the magnetosphere during M2 was extremely dynamic
366 (Slavin et al., 2009), yet the exospheric consequences of short-term (~1 min)
367 magnetospheric variability due to magnetic reconnection have not been evaluated by any
368 model to date. Bearing these uncertainties in mind, we conclude that, although sizeable,
369 the contributions by sputtering alone cannot provide the entire energetic component and
370 so the MESSENGER measurements indicate that some other energetic source process is
371 at play.
372
373 *4.3. Impact vaporization*
374
375 To first order the influx of micrometeoroids to Mercury's surface is assumed to be
376 isotropic. We model the production of atomic magnesium during impacts as following a
377 Maxwellian distribution at temperatures 3,000–5,000 K. Under the assumption that
378 meteoroid impacts produce both atoms and molecules, we include in our simulations the
379 dissociation products of $MgO \rightarrow Mg + O$. Three unknowns are the dissociation cross
380 sections, the resulting velocity distribution of the dissociated ejecta, and the molecule
381 lifetime.

382 Lacking experimental results, we assume that the molecules dissociate due to their
383 high internal energy (they are hot, hence unstable, if they are produced during impacts).
384 In this case, a wide spectrum of ejecta energies can be expected, so our assumed
385 energetic Mg distributions from dissociation are Maxwellian at equivalent temperatures
386 of at least 5,000 K (> 0.5 eV). The dissociation lifetime τ of MgO may be very short, 4 s
387 according to scalings from other diatomic molecules (Berezhnoy, 2010). However,
388 metallic oxides in Earth's atmosphere are fairly stable, with a known lifetime for NaO of
389 42 s (Self and Plane, 2002). In this Section we present models in which the molecule is
390 assumed to break up immediately upon production ($\tau = 0$) and the exobase is Mercury's
391 surface; in the following section we present models with finite τ, where the exobase is
392 extended.

Sean Solomon 5/4/11 9:40 AM
Comment: Menelaos, you did not include this reference in the References. I have guessed the paper you intended.

Menelaos Sarantos 5/4/11 9:46 AM
Comment: Sean, you guessed right—thank you.

393 If $\tau = 0$ and sputtering contributions are small, then we effectively recover the two-
394 component Chamberlain fits (see Table 1) for the partitioning of atoms and molecules in
395 the vapor. A match between the model results and the magnesium measurements in the
396 fantail and near-terminator regions, fit together to describe the global distribution of
397 magnesium self-consistently, is shown in Fig. 5, where "Model Sum" refers to the total
398 contribution by sputtered magnesium, impact-driven atomic magnesium, and magnesium
399 from dissociation. We also ran models where the molecules were allowed to dissociate
400 only on the dayside and beyond the shadow (photolytic scenario), and found, in that case,
401 that the molecule production rates must be about a factor of three higher than the rates
402 quoted in Table 1 to put the same number of atoms in the tail. As in Section 3, the wide
403 range of possible values for these sources can be traced to measurement uncertainties
404 because pairwise combinations of all models differ by statistically insignificant amounts.
405 In summary, we conclude that the high-altitude measurements can be explained by the
406 processes studied here if approximately one-third to one-half of the total amount of

407 exospheric magnesium due to impacts comes directly in atomic form, and the rest results
408 from the dissociation of a molecule, with the total rate summing to (2– 4) × 10^6 Mg
409 atoms cm^{-2} s^{-1} if the molecule photolyzes, or to about (1– 2) × 10^6 Mg atoms cm^{-2} s^{-1} if
410 the molecule vibrationally dissociates.
411 [Insert Fig. 5]
412 Can impact vaporization rates produce the observed tail abundances? The total vapor
413 rate produced by micrometeoroid impacts at 0.342 AU was estimated by Killen et al.
414 (2010) to be M_{vap} = 2.7 × 10^7 atoms cm^{-2} s^{-1} for all species. The model is based on the
415 assumption that the delivery of meteoroid material at Earth's vicinity is at a rate of 3 × 10
416 $^{-16}$ g cm^{-3} for particles smaller than 1 cm (Love and Brownlee, 1993); this rate can be
417 scaled to Mercury's distance from the Sun, 0.342 astronomical units (AU) at the time of
418 the second MESSENGER flyby, following Cintala (1992); and the thermodynamic
419 parameters of aluminum onto enstatite and a regolith porosity of 0.5 (Morgan and Killen,
420 1997; Killen et al., 2005) may be adopted. On assuming a magnesium abundance in the
421 regolith between the lunar values and those recently estimated for Mercury's regolith by
422 Wurz et al. (2010), c = 0.05 – 0.17 by number, we estimate the magnesium production
423 rate due to a uniform micrometeoroid influx to be (1.3–4.7) × 10^6 Mg atoms cm^{-2} s^{-1}.
424 This vaporization rate, which includes the products of MgO if formed in the cloud
425 expansion, is consistent with the rate inferred from the tail measurements, ≤ (2–4) × 10^6
426 Mg atoms cm^{-2} s^{-1}, if the molecule lifetime is very short. A point that will be studied next,
427 and which was not addressed by Killen et al. (2010), regards the effect of a finite
428 molecule lifetime on impact-driven arguments.
429
430 *4.4. Extended exosphere models*

Sean Solomon 3/4/11 9:16 AM
Comment: Menelaos, is "rate" the correct word here, given that you are citing a flux. (See my question at this point in the previous draft.)

If the molecule has a finite lifetime, the required rates will exceed those quoted above because a fraction of the molecule population returns to the surface before it is dissociated. We tested a source of Mg by dissociation of MgO at different altitudes from the surface. We computed the loss flux to dissociation of MgO molecules as a function of altitude, r, having corrected the distribution function $f(r)$ for the survival probability, $e^{-t(r,v)/\tau}$, where $t(r,v)$ is the time elapsed since ejection from an altitude r_0 and τ the molecule lifetime (e.g., Cui et al., 2008). This loss flux, which is the production rate of new atoms, was used to initialize the atom redistribution model of Eq. 2 where the limits of integration now relate to jumps both from higher and from lower altitudes. The molecule lifetime was treated as a free parameter with an assumed range between 1-1000 s.

Sean Solomon 3/4/11 10:16 AM
Comment: Menelaos, it is not a good idea to have boldface **r** denote radius and italicized r denote altitude. I suggest that the pick a different symbol for altitude, say, z or h.

In the right panel of Fig. 6 we present profiles of the dissociating flux from an MgO molecule produced from the surface at a rate of 10^6 molecules cm^{-2} s^{-1}. On the left the resulting profiles for energetic Mg atoms are shown, along with the $\tau = 0$ profile at the same rate and dissociation temperature. It can be seen that: (1) the profiles from an extended exosphere are less steep, meaning that particles can escape easier from a given altitude at the same assumed dissociation temperature; (2) at $\tau = 1$ s the model approaches the idealized $\tau = 0$ model of the previous section, and (3) if the molecules are stable, higher ejection rates are necessary to populate the tail with the same number of atoms. With the exception of the production rate, the profiles are so similar that we cannot separate the effects of a different temperature of the original molecule (T = 3000 – 5000 K), the different dissociation temperatures (5000 – 20000 K tested), and the different lifetime τ.

menelaos sarantos 3/4/11 9:18 AM
Comment: Sean, is this a clear answer to your question?

Two questions that we can now answer are: can the surface limit the delivery rate of magnesium to the exosphere? And what is the possible lifetime of the putative Mg-

457 bearing molecule? A limit to the rate that the surface can provide is the gardening rate.
458 For a turnover rate at Mercury that is ten times that of the Moon, the top μm is turned
459 over once every 125 years; this rate brings ~6×10^7 new Mg atoms cm^{-2} s^{-1} over such a
460 time to the upper μm, which is the depth from which impact vaporization draws its
461 supply. This rate exceeds the exospheric rates by more than an order of magnitude if the
462 molecule has an infinitesimal lifetime (see previous Section). If τ is longer, our
463 simulations indicate that:

464 • For τ = 1000 s the required source rates to populate the tail exceed the
465 gardening rate.
466 • For τ = 100 s the data necessitate a rate of (2–5) $\times10^7$ mol cm^{-2} s^{-1}, i.e., less
467 than the gardening rate but up to 10 times the impact vaporization rate given
468 by Cintala (1992).
469 • For τ = 10 s a best fit requires (3–7) $\times10^6$ mol cm^{-2} s^{-1}, no more than three
470 times the rate quoted in the previous Section.

471 Our prediction of short dissociation lifetimes for MgO can be tested with laboratory
472 experiments.
473
474 **5. Magnesium near the surface**
475
476 We can approximately reproduce the magnesium tail under the assumption that the
477 source processes are sputtering and uniform impact-driven release, but we cannot
478 reproduce the distribution near the terminator where half the exospheric content is not
479 predicted by these processes (compare Fig. 5b to Fig. 3). Because of observational
480 constraints, we cannot ascertain what causes the enhancements observed in this region.
481 We suggest two possibilities that may explain the magnesium distribution near the

482 planetary surface: one relating to a local source of impacts (Section 5.1), and one relating
483 to a reservoir of adsorbed particles (Section 5.2).
484
485 *5.1. A single ~0.5 m impactor at equatorial dawn?*
486
487 We can visualize what is inherently different about the measurements obtained near
488 the dawn terminator by mapping with our particle transport model the "footprint" of
489 atoms that scatter light into the instrument for different boresights and tangent heights.
490 Some examples are shown in Fig. 7 for a uniform source having temperature T = 5,000 K.
491 [Insert Fig. 7]
492 For lines of sight pointing far from the surface (in the tail and fantail observations),
493 MESSENGER UVVS observed primarily the escaping component; hence the
494 instrument's effective field of view is large. Fig. 7a shows a typical measurement
495 obtained in the tail prior to the spacecraft entering the shadow, and Figs. 7b to 7d show
496 the beginning, middle, and end of the fantail sequence. As expected, the main
497 contributions to the observed column abundance drift from being approximately equally
498 weighted between dawn and dusk in the tail to being primarily dawn, then north, then
499 dusk during the fantail sequence. Particles mapping outside the shadow originate mainly
500 from the nightside surface and contribute approximately two-thirds of the Chamberlain
501 column abundance; ~one-third of the total column abundance is contributed by particles
502 originating on the dayside. (This result implies that the molecule production rates quoted
503 in the paper should be increased by a factor of three if the molecule is destroyed by
504 photons rather than being vibrationally dissociated.). As a wide area of the surface

505 contributes to the tail and fantail measurements, localized "disturbances" such as a
506 surface density enhancement or a meteoroid impinging on Mercury's near-equatorial,
507 morning sector would go undetected until the spacecraft pointed near the surface.

508 In contrast, for lines of sight nearly intercepting the dawn terminator surface, the
509 ejecta mapping into the instrument's field of view are very localized. As the spacecraft
510 comes out of the shadow, the population sampled is slowly drifting towards the equatorial
511 dawn and morning sectors in successive lines of sight (Fig. 7e – f). We conclude that the
512 measurements near the terminator are sensitive to localized sources. This point is further
513 studied in Fig. 8.

514 Having evaluated the impact-driven column abundances element by element as in Fig.
515 7, we then combine them by different amounts to investigate possible asymmetries in a
516 least-squares manner. First, we determine the location of the possible meteoroid impact
517 by iteratively enhancing the weight of "pixels" starting at equatorial dawn, then
518 progressively expanding the "size" of the assumed impact area. The shape of the near-
519 terminator curve is fit best if we enhance only one pixel, that sitting at the dawn
520 terminator with an extent of ± 10° in longitude and latitude. Then, the production rate and
521 its partitioning into the two impact-driven populations is determined by least-squares
522 regression. This outcome is shown in Fig. 8 for assumed local enhancements of vapor
523 rates over the uniform model by factors of four and eight. As seen in the left column,
524 these models are indistinguishable from fantail measurements, but the models having
525 enhancement factors of 4–8 represent the near-terminator observations increasingly well.
526 [Insert Fig. 8]

527 A meteoroid stream is not a suitable explanation because streams would be expected
528 to have a hemispherical dependence and not be so localized (J. Vaubaillon, personal
529 communication, 2010). A single impactor in a small region around dawn is possible.
530 According to our estimates, enhancements of the local impact-driven release rate by
531 factors of 4–8 would require the meteoroid to have a diameter of ~0.3 m; impacts of
532 objects of such a size occur once every 3-4 days at Mercury. The likelihood that this
533 impact happened around dawn within ~1000 s prior to this observation so that the cloud
534 remained localized is low.
535
536 *5.2. A source of volatile Mg?*
537
538 An alternative, more likely way to interpret the near-terminator measurements is to
539 assume that returning Mg atoms from an energetic process do not strongly bind with the
540 surface and can be re-emitted to the gas phase when exposed to UV photons or to the
541 high temperatures of the dayside surface. Such a hypothesis is suggested by the two-
542 component Chamberlain fits (Section 3). As illustrated by Fig. 3, a low-energy source
543 produces a sharp increase in column abundance as the spacecraft probes areas near the
544 planet, i.e., within 100 km of the surface. Note, however, that the population consistent
545 with a T = 400 K Chamberlain model would be effectively concentrated on the nightside
546 during this sequence (e.g., see Fig. 7).
547 A source concentrated on the dayside would produce the same sharp exospheric
548 profile over the terminator but would require much higher source rates than those of a
549 uniform model (Table 1). To investigate the possibility that the terminator measurements

550 for Mg might be consistent with photon-stimulated desorption (PSD) or thermal
551 desorption of adsorbed ejecta, we ran models under the premise that, in addition to
552 uniform impact vaporization of atoms and molecules, sources included a dayside source
553 having a cos (χ) or $\cos^{1/4}$ (χ) dependence on the solar zenith angle, χ, a varying
554 temperature of 100-1500 K, and no emission from the nightside. We found excellent fits
555 to the observed profile for assumed source temperatures of ~700-1200 K. However, the
556 required rates to match the measurements with these dayside source models were too
557 high, 5×10^8 Mg atoms cm^{-2} s^{-1}, to be provided either by the return rate or by the
558 gardening rate; such rates can be justified only if returning particles do not stick and
559 rebound multiple times, which is probably a poor assumption for refractory elements
560 such as Mg.

561 In conclusion, the illuminated limb-scan profiles can be matched at acceptable
562 source rates only if the putative cold source extends to the nightside. That is, some
563 process other than PSD and thermal desorption would be required to eject low-energy Mg
564 neutrals. Perhaps electron-stimulated desorption (ESD) is responsible for T = 400 K
565 neutrals since magnetospheric electrons have access to the nightside; no ESD
566 measurements are available for this species, however. Note that the inferred rate from a
567 T = 400 K source corresponds to a few times 10^6 atoms cm^{-2} s^{-1} (Table 1). Although our
568 simulations have not carefully treated the reservoir in the top monolayer of the surface,
569 flux of this magnitude could approximately be provided by the return rate of impact-
570 driven atomic Mg and by surface-directed Mg from dissociation of a molecule with a
571 finite lifetime. All but 1–2 % of magnesium atoms from a 3000–5000 K source are

572 gravitationally bound, and approximately half the dissociating flux from a molecule will
573 be directed towards the surface.
574
575 **6. Conclusions**
576
577 Comparison of the measurements of Mg in Mercury's exosphere with a large number of
578 simulations have suggested the following possibilities: (1) scale-height arguments imply the
579 presence of at least two distinct temperatures; (2) energetic processes, such as
580 micrometeoroid impact vaporization, ion sputtering, and dissociation of a Mg-bearing oxide,
581 can supply the exospheric population at high altitudes, but no single process dominates; (3)
582 the lifetime of the putative molecule may not exceed ~100 s in order to supply the needed
583 rates given the replenishment rates of the surface by gardening; and (4) at low altitudes, low-
584 energy processes appear to act on a limited reservoir of volatiles that may be provided by
585 recycled atoms from hot processes. A visual summary of the paper's results appears in Fig. 9.
586 Preliminary analysis of third flyby data (not discussed at length in this paper)
587 indicates similar temperatures and source rates in the tail and polar regions to those
588 presented here. We cannot confirm the volatile source because observations of
589 magnesium on the equatorial dawn region were not conducted by MESSENGER during
590 its third flyby as a result of a spacecraft safe-hold event (Vervack et al., 2010).
591 Improvements to the model will require laboratory measurements of appropriate physical
592 constants (e.g., molecule lifetime and dissociation cross-sections, and temperature-
593 programmed desorption yields for adsorbed Mg). The measurements expected during the
594 orbital phase of the MESSENGER mission promise to further constrain these results. For
595 instance, if impacts populate the high-altitude Mg exosphere as inferred here, there

should be a correlation of exospheric content with spacecraft passages through the interplanetary dust plane (Kameda et al., 2009). A source of volatiles can be verified or refuted during repeated illuminated limb-scanning opportunities.

Acknowledgments. The MESSENGER project is supported by the NASA Discovery Program under contracts NAS5-97271 to the Johns Hopkins University Applied Physics Laboratory and NASW-00002 to the Carnegie Institution of Washington. RMK, RJV, and MB are supported by the MESSENGER Participating Scientist Program. MS thanks Apostolos Christou and Jeremie Vaubaillon for their remarks on the possibility that a meteoroid stream affected Mercury during the flyby observations, and Richard Hartle for his suggestions on modeling exospheric dissociating ejecta.

607 **References**

608

609 Benna, M., Anderson, B.J., Baker, D.N., Boardsen, S.A., Gloeckler, G., Gold, R.E., Ho,
610 G.C., Killen, R.M., Korth, H., Krimigis, S.M., Purucker, M.E., McNutt, R.L., Jr.,
611 Raines, J.M., McClintock, W.E., Sarantos, M., Slavin, J.A., Solomon, S.C.,
612 Zurbuchen, T.H., 2010. Modeling of the magnetosphere of Mercury at the time of the
613 first MESSENGER flyby. Icarus 209, 3–10.

614 Berezhnoy, A.A., 2010. Meteoroid bombardment as a source of the lunar exosphere. Adv.
615 Space Res. 45, 70–76.

616 Berezhnoy, A.A., Klumov, B.A., 2008. Impacts as sources of the exosphere on Mercury.
617 Icarus 195, 511–522.

618 Burger, M.H., Killen, R.M., Vervack, R.J., Jr., Bradley, T.E., McClintock, W.E.,
619 Sarantos, M., Benna, M., Mouawad, N., 2010. Monte Carlo modeling of sodium in
620 Mercury's exosphere during the first two MESSENGER flybys. Icarus 209, 63–74.

621 Chamberlain, J.W., 1963. Planetary coronae and atmospheric evaporation. Planet. Space
622 Sci. 11, 901–960.

623 Cintala, M.E., 1992. Impact-induced thermal effects in the lunar and Mercurian regoliths.
624 J. Geophys. Res. 97, 947–973.

625 Cui, J., Yelle, R.V., Volk, K., 2008. Distribution and escape of molecular hydrogen in
626 Titan's thermosphere and exosphere. J. Geophys. Res. 113, E10004,
627 doi:10.1029/2007JE003032.

628 Eichorn, G., 1978. Heating and vaporization during hypervelocity particle impact. Planet.
629 Space Sci. 26, 463–467.

Comment: Menelaos, in PSS journal names are not set in italics, no comma precedes the volume number, and volumes numbers are neither in italics or boldface.

630 Hartle, R.E., 1971. Model for rotating and nonuniform planetary exospheres. Phys. Fluids
631 14, 2592–2598.
632 Kameda, S., Yoshikawa, I., Kagitani, M., Okano, S., 2009. Interplanetary dust
633 distribution and temporal variability of Mercury's atmospheric Na. Geophys. Res.
634 Lett. 36, L15201, doi:10.1029/2009GL039036.
635 Killen, R.M., Potter, A.E., Reiff, P., Sarantos, M., Jackson, B.V., Hick, P., Giles, B.,
636 2001. Evidence for space weather at Mercury. J. Geophys. Res. 106, 20509–20526.
637 Killen, R.M., Sarantos, M., Potter, A.E., Reiff, P.H., 2004. Source rates and ion recycling
638 rates for Na and K in Mercury's atmosphere. Icarus 171, 1–19.
639 Killen, R.M., Bida, T.A., Morgan, T.H., 2005. The calcium exosphere of Mercury. Icarus
640 173, 300–311.
641 Killen, R.M., Cremonese, G., Lammer, H., Orsini, S., Potter, A.E., Sprague, A.L., Wurz,
642 P., Khodachenko, M.L., Lichtenegger, H.I.M, Milillo, A., Mura, A., 2007. Processes
643 that promote and deplete the atmosphere of Mercury. Space Sci. Rev. 132, 433–509.
644 Killen, R.M., Shemansky, D., Mouawad, N., 2009. Expected emission from Mercury's
645 exospheric species, and their ultraviolet-visible signatures. Astrophys. J. Suppl. Ser.
646 181, 351–359.
647 Killen, R.M., Potter, A.E., Vervack, R.J., Jr., Bradley, E.T., McClintock, W.E.,
648 Anderson, C.M., 2010. Observations of metallic species in Mercury's exosphere.
649 Icarus 209, 75–87.
650 Leblanc, F., Johnson, R.E., 2010. Mercury exosphere I. Global circulation model of its
651 sodium component. Icarus 209, 280–300.

652 Love, S.G., Brownlee, D.E., 1993. A direct measurement of the terrestrial mass
653 accretion rate of cosmic dust. Science 262, 550–553.
654 McClintock, W.E., Bradley, E.T., Vervack, R.J., Jr., Killen, R.M., Sprague, A.L.,
655 Izenberg, N.R., Solomon, S.C., 2008. Mercury's exosphere: observations during
656 MESSENGER's first Mercury flyby. Science 321, 92–94.
657 McClintock, W.E., Vervack, R.J. Jr., Bradley, E.T., Killen, R.M., Mouawad, N., Sprague,
658 A.L., Burger, M.H., Solomon, S.C., Izenberg, N.R., 2009. MESSENGER
659 observations of Mercury's exosphere: detection of magnesium and distribution of
660 constituents. Science 324, 610–613.
661 Milillo, A., Fujimoto, M., Kallio, E., Kameda, S., Leblanc, F., Narita, Y., Cremonese, G.,
662 Laakso, H., Laurenza, M., Massetti, S., McKenna-Lawlor, S., Mura, A.,
663 Nakamura, R., Omura, Y., Rothery, D.A., Seki, K., Storini, M., Wurz, P.,
664 Baumjohann, W., Bunce, E.J., Kasaba, Y., Helbert, J., Sprague, A.L., 2010. The
665 BepiColombo mission: an outstanding tool for investigating the Hermean
666 environment. Planet. Space Sci. 58, 40–60.
667 Morgan, T.H., Killen, R.M., 1997. A non-stoichiometric model of the composition of the
668 atmospheres of Mercury and the Moon. Planet. Space Sci, 45, 81–94.
669 Morgan, T.H., Zook, H.A., Potter, A.E., 1988. Impact-driven supply of sodium and
670 potassium to the atmosphere of Mercury. Icarus 75, 156–170.
671 Mouawad, N., Burger, M.H., Killen, R.M., Potter, A.E., Naidu, S., McClintock, W.E.,
672 Vervack, R.J. Jr., Bradley, E.T., 2011. Constraints on Mercury's sodium exosphere:
673 Combined MESSENGER and ground – based data. Icarus 211, 21–36.

674 Mura, A., Wurz, P., Lichtenegger, H.I.M., Schleicher, H., Lammer, H., Delcourt, D.,
675 Milillo, A., Orsini, S., Massetti, S., Khodachenko, M.L., 2009. The sodium exosphere
676 of Mercury: comparison between observations during Mercury's transit and model
677 results. Icarus 200, 1–11.
678 Sarantos, M., Reiff, P.H., Hill, T.W., Killen, R.M., Urquhart, A.L., 2001. A B_x-
679 interconnected magnetosphere model for Mercury. Planet. Space Sci. 49, 1629–1635.
680 Sarantos, M., Killen, R.M., Kim, D., 2007. Predicting the long-term solar wind ion-
681 sputtering source at Mercury. Planet. Space Sci. 55, 1584–1595.
682 Sarantos, M., Killen, R.M., Sharma, A.S., Slavin, J.A., 2010. Sources of sodium in the
683 lunar exosphere: modeling using ground-based observations and spacecraft data of
684 the plasma. Icarus 205, 364–374.
685 Self, D.E., Plane, J.M.C., 2002. Absolute photolysis cross-sections for $NaHCO_3$, NaOH,
686 NaO, NaO_2 and NaO_3: implication for sodium chemistry in the upper mesosphere.
687 Phys. Chem. Chem. Phys. 4, 16–23.
688 Slavin, J.A., Acuña, M.H., Anderson, B.J., Baker, D.N., Benna, M., Boardsen, S.A.,
689 Gloeckler, G., Gold, R.E., Ho, G.C., Korth, H., Krimigis, S.M., McNutt, R.L., Jr.,
690 Raines, J.M., Sarantos, M., Schriver, D., Solomon, S.C., Trávníček, P.,
691 Zurbuchen, T.H., 2009. MESSENGER observations of magnetic reconnection in
692 Mercury's magnetosphere. Science 324, 606–610.
693 Solomon, S.C., McNutt, R.L., Jr., Gold, R.E., Acuña, M.H., Baker, D.N., Boynton, W.V.,
694 Chapman, C.R., Cheng, A.F., Gloeckler, G., Head, J.W., III, Krimigis, S.M.,
695 McClintock, W.E., Murchie, S.L., Peale, S.J., Phillips, R.J., Robinson, M.S., Slavin,
696 J.A., Smith, D.E., Strom, R.G., Trombka, J.I., Zuber, M.T., 2001. MESSENGER

mission to Mercury: scientific objectives and implementation. Planet. Space Sci. 49, 1445–1460.

Vervack, R.J., Jr., McClintock, W.E., Killen, R.M., Sprague, A.L., Anderson, B.J., Burger, M.H., Bradley, E.T., Mouawad, N., Solomon, S.C., Izenberg, N.R., 2010. Mercury's complex exosphere: results from MESSENGER's third flyby. Science 329, 672–675.

Wurz, P., Rohner, U., Whitby, J.A., Kolb, C., Lammer, H., Dobnikar, P., Martín-Fernández, J.A., 2007. The lunar exosphere: the sputtering contribution. Icarus 191, 486–496.

Wurz, P., Whitby, J.A., Rohner, U., Martín-Fernández, J.A., Lammer, H., Kolb, C., 2010. Self-consistent modelling of Mercury's exosphere by sputtering, micro-meteorite impact and photon-stimulated desorption. Planet. Space Sci. 58, 1599–1616.

Table 1. Two-component Chamberlain models obtained by superposing a cool source, 100-5000 K, and a hot source, $T \geq 10000$ K.

Model: $n_{0,LT}\, I(T=3000\ K) + n_{0,HT}\, I(T)$					
$n_{0,LT}$ (atoms cm^{-3})	T ($\times 10^3$ K)	$n_{0,HT}$ (atoms cm^{-3})	S_{LT} ($\times 10^5$ cm^{-2} s^{-1})	S_{HT} ($\times 10^6$ cm^{-2} s^{-1})	χ^2/ν
6.1	10	12.7	2.4	0.9	6.23
14.8	20	8.7	6.0	1.0	5.48
16.8	30	8.5	6.8	1.1	5.29
17.7	40	8.7	7.2	1.3	5.20
18.1	50	9.0	7.4	1.5	5.15
Model: $n_{0,LT}\, I(T=400\ K) + n_{0,HT}\, I(T)$					
$n_{0,LT}$ (atoms cm^{-3})	T ($\times 10^3$ K)	$n_{0,HT}$ (atoms cm^{-3})	S_{LT} ($\times 10^6$ cm^{-2} s^{-1})	S_{HT} ($\times 10^6$ cm^{-2} s^{-1})	χ^2/ν
298	10	12.1	4.4	0.9	5.87
397	20	9.0	5.9	0.9	5.03
418	30	8.9	6.2	1.1	4.84
426	40	9.2	6.3	1.4	4.75
430	50	9.5	6.4	1.6	4.71

Notes: Listed are the corresponding surface density, n_0, production rate, S, and reduced chi squared error, χ^2/ν, for different assumed values of the exobase temperature, T. The models are fit to all measurements. (LT=Low Temperature; HT = High Temperature)

718
719 Figure Captions

720

721 **Fig. 1.** All Mg observations obtained during MESSENGER's second flyby were fit to
722 Chamberlain models. Shown here are lines of sight through the tail that intercept the
723 noon-midnight meridian plane (a) 2 to 4 R_M from the equatorial plane; (b) 1 to 2 R_M from
724 the equator; and (c) inside Mercury's shadow. The measurements and their uncertainties
725 are shown in red. Three models shown, which have temperatures of 3,000 (dotted black
726 line), 20,000 (blue line) and 50,000 K (magenta line), indicate that atoms in the tail are
727 very energetic.

728

729 **Fig. 2.** Weighted least-squared fits of (a) the fantail and (b) near-terminator
730 measurements to Chamberlain models subject also to the tail data. Only a poor
731 description of the low-altitude measurements near dawn can be achieved with a single
732 temperature.

733

734 **Fig. 3.** Two-component models are improvements over single-component models at low
735 altitudes, especially if a low-energy source (T = 400 K) is assumed (panels c and d). The
736 fantail observations, where the line of sight drifts to infinity, constrain the energetic
737 process, whereas the source having the smaller temperature dominates the near-
738 terminator measurements, which probe altitudes near the surface.

739

740 **Fig. 4.** (a) The adopted location and flux of protons bombarding the surface of Mercury,
741 obtained from a MHD model of Mercury's magnetosphere (Benna et al., 2010); (b)
742 amount of magnesium that can be attributed to sputtering under these conditions.
743
744 **Fig. 5.** A possible model of Mercury's magnesium exosphere consisting of three assumed
745 source processes: sputtering (in green), impact vaporization of atomic Mg (in black), and
746 dissociation of MgO (in blue). In contrast to the model shown in the next figure, here the
747 molecule is assumed to break up immediately upon production ($\tau = 0$). In this limiting
748 case the inferred rates can be provided by impact vaporization of atoms and molecules for
749 magnesium abundances in the regolith of five percent or higher. The sputtering
750 contribution to the near-terminator measurements is below the scale shown.
751
752 **Fig. 6.** (a) Flux of dissociating MgO as a function of radial distance and an assumed
753 molecule lifetime, τ, as the source rate for an extended exosphere model; (b) profiles of
754 energetic Mg resulting from the dissociation of MgO with arbitrary τ. A production rate
755 of 10^6 molecules cm^{-2} s^{-1} and a dissociation temperature of 20,000 K are assumed; $\tau = 0$
756 is the profile used in the simplified case of Fig. 5 at the same temperature. Ejection rates
757 of a stable molecule must evidently be higher in order to produce the same column
758 abundance in the tail. Based on a comparison to the gardening rate, the molecule must be
759 short-lived, $\tau \leq 2$ min, to explain the measurements.
760
761 **Fig. 7.** Relative contribution by planetary surface elements to the modeled column
762 abundance for an isotropic impact vaporization source ($T = 5000$ K) and for selected lines

763 of sight: (a) typical line through the equatorial tail when the spacecraft lies outside the
764 shadow; (b)-(d) the beginning, mid-point, and end of the fantail sequence; (e)-(f) first and
765 last lines of sight for the near-terminator sequence. In these plots, the integrated column
766 abundance from a model of uniform ejection has been divided to extract the originating
767 locations of particles that map outside the planetary shadow (and hence contribute to the
768 measurements). The main point illustrated is that particles that affect the pre-dawn
769 observations originate from a limited region nearby. The subsolar point is indicated by
770 the white dot.
771
772 **Fig. 8.** In addition to the assumption of a low-energy source (Fig. 3), models of the near-
773 terminator measurements markedly improve if a single meteoroid impacted Mercury
774 within $\pm 10^{\circ}$ of equatorial dawn around the time of these observations: (upper panel)
775 model with no equatorial enhancement at dawn; (middle panel) model with a factor of
776 four, and (lower panel) model with a factor of eight enhancement over the uniform
777 impact vaporization rate. In each case the "background" surface density, n_0, needed to
778 match the data is shown in black (T = 3000 K) and blue (T = 20,000 K). It is surmised
779 that a single meteoroid should have produced the equivalent flux of ~(6–8) × 10^6
780 atoms/molecules cm^{-2} s^{-1} within a brief period prior to the last few measurements for this
781 scenario to work.
782
783 **Fig. 9.** Schematic depiction of potential processes promoting Mg to the exosphere. The
784 gardening rate in the top micron suffices to provide the exospheric rates, shown here for

785 brief molecule lifetimes. The recycling rate of bound ejecta could replenish an

786 unexpected reservoir of volatiles at rates of ~10^6 atoms cm^{-2} s^{-1}.

787

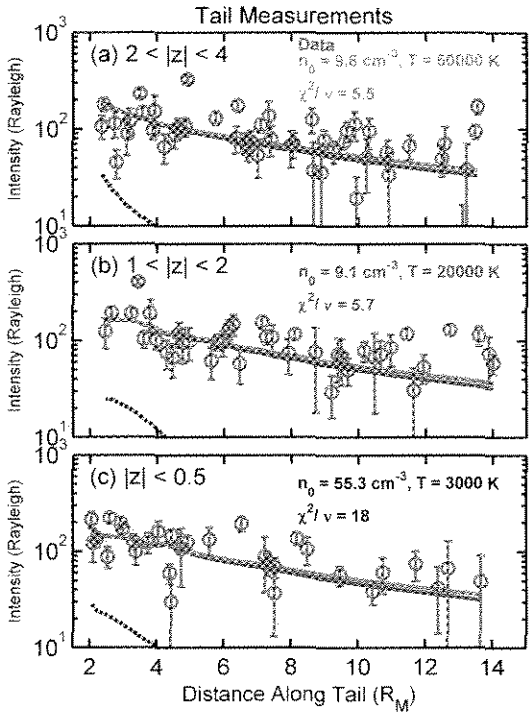

788

789 Figure. 1

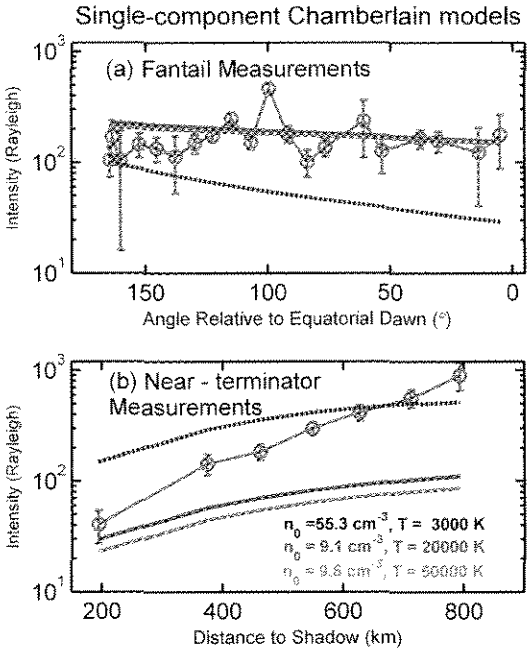

790

791 Figure 2

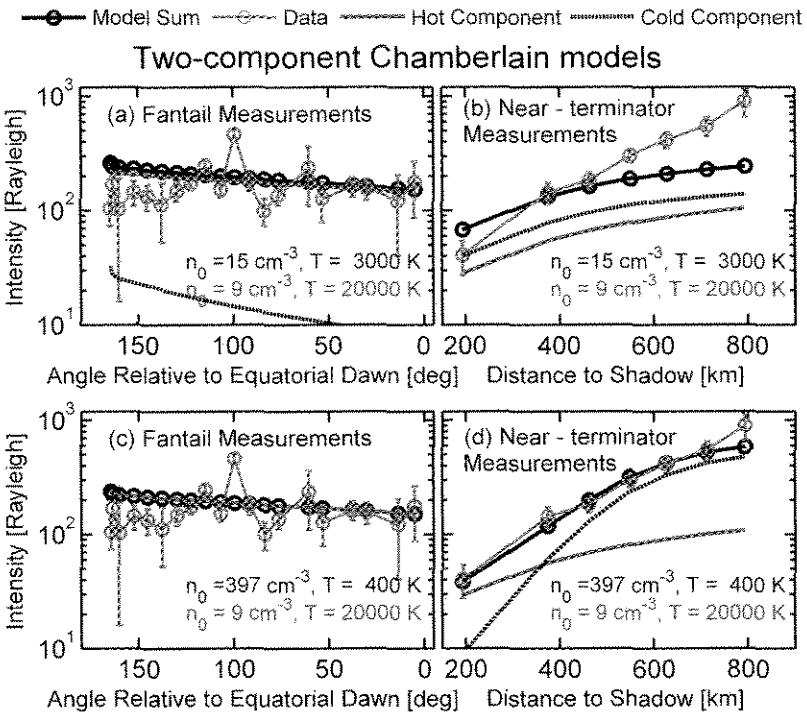

792

793 Figure 3

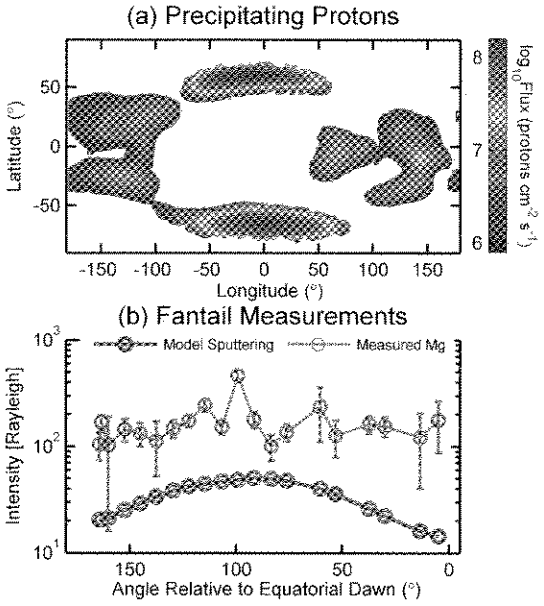

794

795 Figure 4

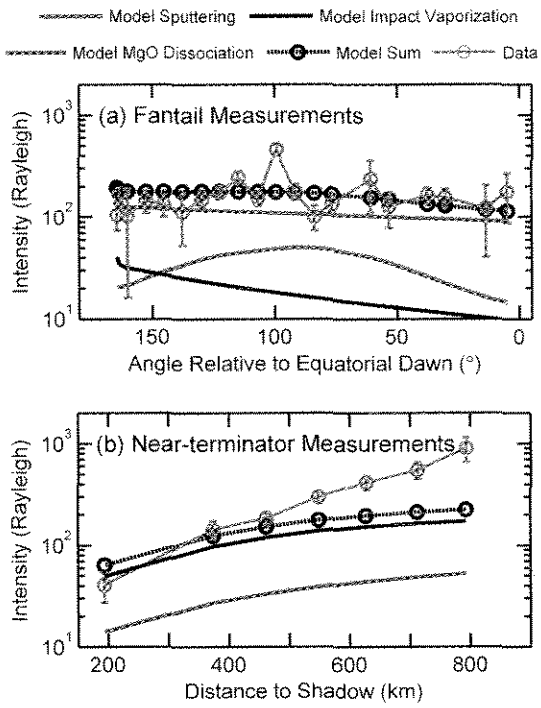

796

797 Figure 5

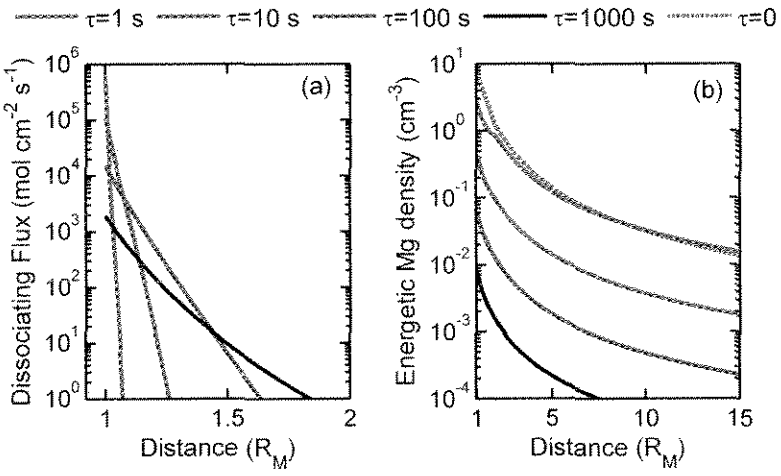

798

799 Figure 6

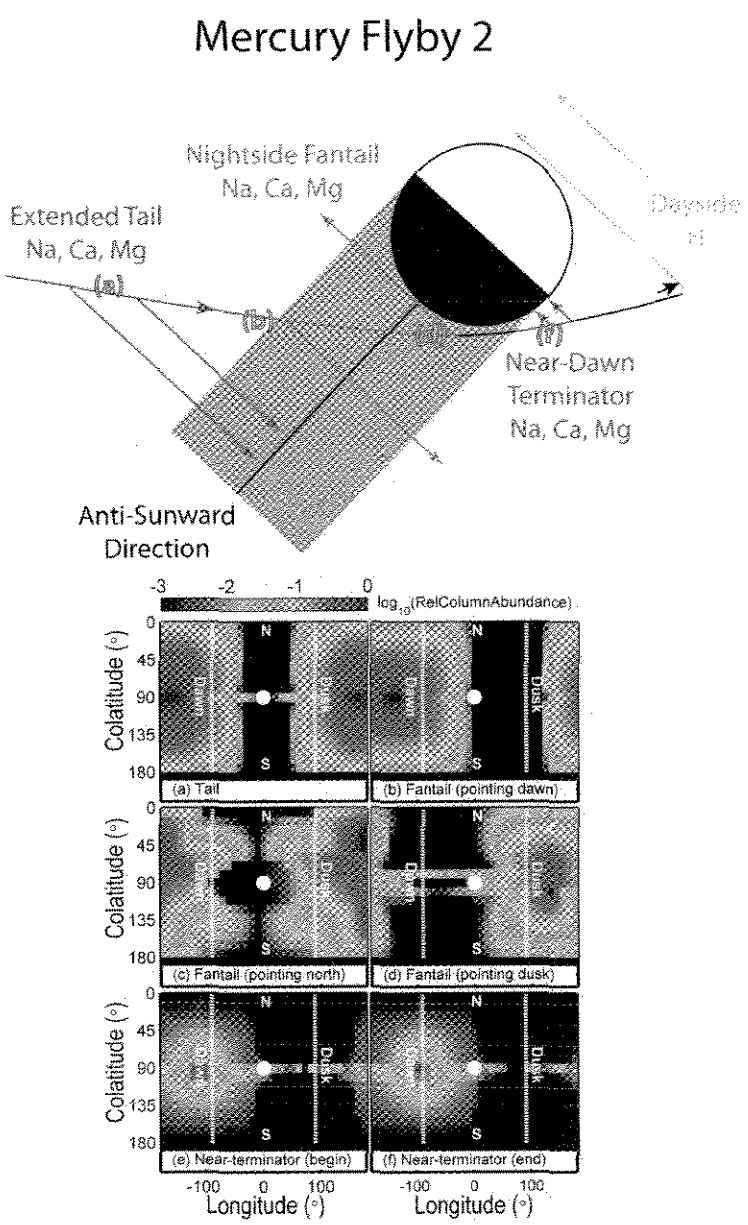

800

801 Figure 7

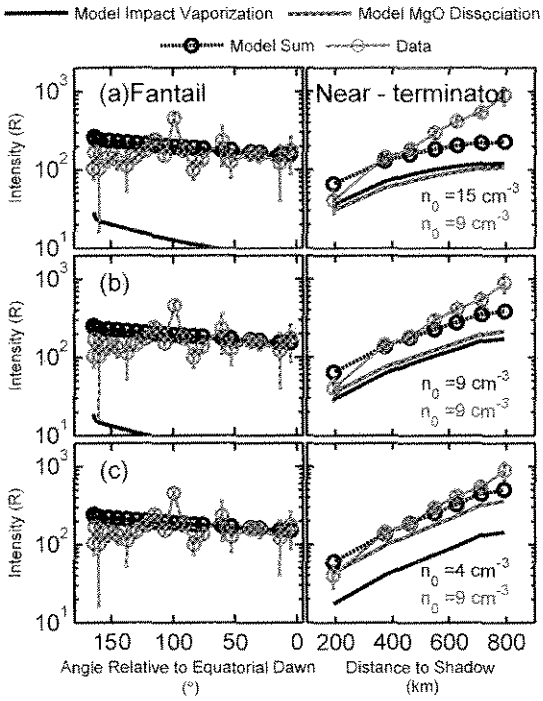

802

803 Figure 8

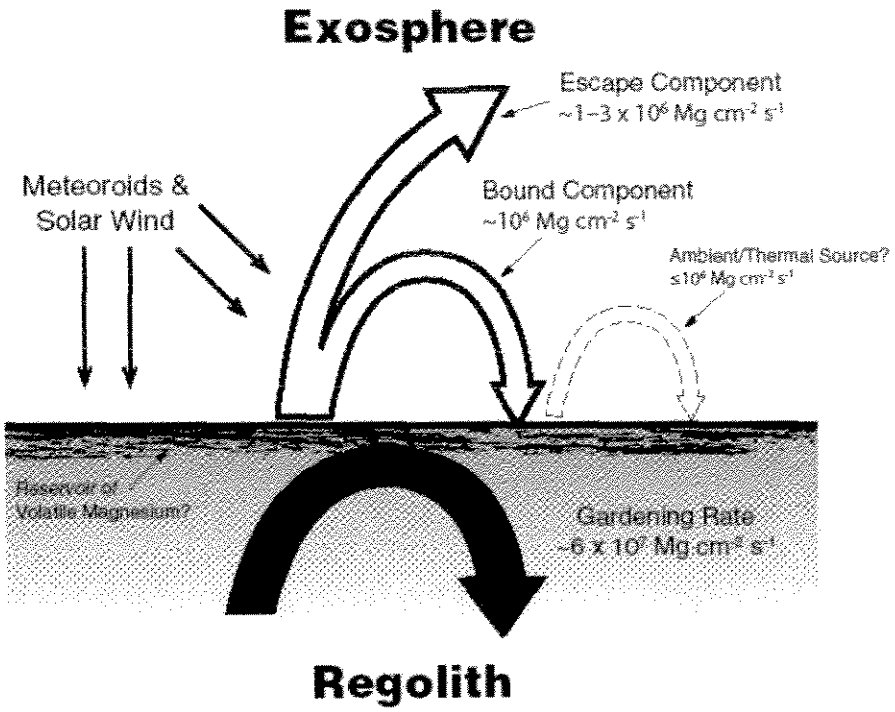

804
805 Figure 9

806